

ACCEPTED MANUSCRIPT

Functional imaging of tumor vasculature using iodine and gadolinium-based nanoparticle contrast agents: a comparison of spectral micro-CT using energy integrating and photon counting detectors

To cite this article before publication: Cristian T Badea *et al* 2019 *Phys. Med. Biol.* in press <https://doi.org/10.1088/1361-6560/ab03e2>

Manuscript version: Accepted Manuscript

Accepted Manuscript is “the version of the article accepted for publication including all changes made as a result of the peer review process, and which may also include the addition to the article by IOP Publishing of a header, an article ID, a cover sheet and/or an ‘Accepted Manuscript’ watermark, but excluding any other editing, typesetting or other changes made by IOP Publishing and/or its licensors”

This Accepted Manuscript is © 2018 Institute of Physics and Engineering in Medicine.

During the embargo period (the 12 month period from the publication of the Version of Record of this article), the Accepted Manuscript is fully protected by copyright and cannot be reused or reposted elsewhere.

As the Version of Record of this article is going to be / has been published on a subscription basis, this Accepted Manuscript is available for reuse under a CC BY-NC-ND 3.0 licence after the 12 month embargo period.

After the embargo period, everyone is permitted to use copy and redistribute this article for non-commercial purposes only, provided that they adhere to all the terms of the licence <https://creativecommons.org/licenses/by-nc-nd/3.0>

Although reasonable endeavours have been taken to obtain all necessary permissions from third parties to include their copyrighted content within this article, their full citation and copyright line may not be present in this Accepted Manuscript version. Before using any content from this article, please refer to the Version of Record on IOPscience once published for full citation and copyright details, as permissions will likely be required. All third party content is fully copyright protected, unless specifically stated otherwise in the figure caption in the Version of Record.

View the [article online](#) for updates and enhancements.

1
2
3 **Functional imaging of tumor vasculature using iodine and gadolinium-based nanoparticle**
4 **contrast agents: a comparison of spectral micro-CT using energy integrating and photon**
5 **counting detectors**
6
7
8
9

10 C. T. Badea^{1*}, D. P. Clark¹, M. Holbrook¹, M. Srivastava³, Y. Mowery², K. B. Ghaghada³

11
12 ¹Center for In Vivo Microscopy, Department of Radiology, Duke University, Durham, NC 27710

13 ²Department of Radiation Oncology, Duke University, Durham, NC 27710

14 ³Singleton Department of Pediatric Radiology, Texas Children's Hospital, Houston, TX 77030,
15 USA.
16
17
18

19 **Keywords:** micro-CT, photon counting detector, preclinical, spectral, contrast agents, liposomes,
20 nanoparticles
21

22 *cristian.badea@duke.edu; phone 1 919 684-7509; <http://www.civm.duhs.duke.edu/>
23
24
25
26
27
28
29
30
31
32
33
34
35
36
37
38
39
40
41
42
43
44
45
46
47
48
49
50
51
52
53
54
55
56
57
58
59
60

ABSTRACT

Advances in computed tomography (CT) hardware have propelled the development of novel CT contrast agents. In particular, the spectral capabilities of X-ray CT can facilitate simultaneous imaging of multiple contrast agents. This approach is particularly useful for functional imaging of solid tumors by simultaneous visualization of multiple targets or architectural features that govern cancer development and progression. Nanoparticles are a promising platform for contrast agent development. While several novel imaging moieties based on high atomic number elements are being explored, iodine (I) and gadolinium (Gd) are particularly attractive because of their existing approval for clinical use. In this work, we investigate the *in vivo* discrimination of I and Gd nanoparticle contrast agents using both dual energy micro-CT with energy integrating detectors (DE-EID) and photon counting detector (PCD)-based spectral micro-CT. Simulations and phantom experiments were performed using varying concentrations of I and Gd to determine the imaging performance with optimized acquisition parameters. Quantitative spectral micro-CT imaging using liposomal-iodine (Lip-I) and liposomal-Gd (Lip-Gd) nanoparticle contrast agents was performed in sarcoma bearing mice for anatomical and functional imaging of tumor vasculature. Iterative reconstruction provided high sensitivity to detect and discriminate relatively low I and Gd concentrations. According to the Rose criterion applied to the experimental results, the detectability limits for I and Gd were approximately 2.5 mg/ml for both DE-EID CT and PCD micro-CT, even if the radiation dose was approximately 3.8 times lower with PCD micro-CT. The material concentration maps confirmed expected biodistributions of contrast agents in the blood, liver, spleen and kidneys. The PCD provided lower background signal and better simultaneous visualization of tumor vasculature and intratumoral distribution patterns of nanoparticle contrast agent compared to DE-EID decompositions. Preclinical spectral CT systems such as this could be useful for functional characterization of solid tumors, simultaneous quantitative imaging of multiple targets and for identifying clinically-relevant applications that benefit from the use of spectral

1
2
3 imaging. Additionally, it could aid in the development nanoparticles that show promise in the
4 developing field of cancer theranostics (therapy and diagnostics) by measuring vascular tumor
5 biomarkers such as fractional blood volume and the delivery of liposomal chemotherapeutics.
6
7
8
9

10 11 1. INTRODUCTION

12
13 Spectral X-ray CT (e.g. dual energy CT) using heavy-metal nanoparticle (NP) contrast agents can
14 facilitate *in vivo* understanding of tumor biology and its relationship to the delivery of NPs for
15 therapy. For instance, two NP contrast agents can be used simultaneously to image tumor
16 'leakiness' and to denote tumor vasculature at high spatial resolution (Clark *et al.*, 2013). Our group
17 has been a pioneer in the preclinical development of DE micro-CT for cancer imaging (Ashton *et*
18 *al.*, 2016; Badea *et al.*, 2012b; Badea *et al.*, 2011). Unfortunately, the contrast sensitivity of DE
19 micro-CT methods is limited by the energy integrating detectors (EIDs) used in most micro-CT
20 instruments. X-rays are composed of photons, and are generally produced with a polychromatic
21 energy spectrum (like visible light). EIDs produce an output signal that is proportional to the
22 detected photon flux, weighted by the photon energy and integrated across the entire photon
23 spectrum. However, heavy-metal contrast agents are differentiable due to spectrally localized
24 changes in X-ray attenuation at characteristic K-edge energies. Thus, the suitability of EIDs for K-
25 edge NP imaging is limited.
26
27
28
29
30
31
32
33
34
35
36
37
38
39

40 Expanding from DE-EID CT to spectral CT using photon counting detectors (PCD) has the
41 potential to improve CT contrast sensitivity (Taguchi and Iwanczyk, 2013). PCDs count and bin X-
42 rays into a number of energy bins and eliminate dark noise in the image by rejecting all counts
43 below the signal. Most importantly, spectral PCD-based CT is expected to provide better material
44 separation compared to DE-EID CT. Clinical use of PCDs remains limited due to pulse pile up and
45 charge sharing effects (Taguchi and Iwanczyk, 2013), though some clinical prototypes already
46 exist (Li *et al.*, 2016). Nevertheless, PCDs could be the next step in CT imaging technology, and
47 their adoption could lead to increases in contrast sensitivity, while reducing radiation exposure
48
49
50
51
52
53
54
55
56
57
58
59
60

1
2
3 during routine CT scans (Symons *et al.*, 2017). Preclinical imaging represents an excellent
4 development and testing environment for spectral PCD CT technologies with potential for clinical
5 translation. Preclinical micro-CT may be less affected by pulse pile-up problems than clinical CT,
6 since the flux can be reduced. Many groups, including ours, are therefore developing new
7 prototype PCD micro-CT systems and new contrast agents to explore their capabilities. Currently,
8 there is one commercially available PCD-based micro-CT system, the Medipix All Resolution
9 System (MARS Bioimaging Ltd.; Christchurch, New Zealand) (Anderson *et al.*, 2010). The MARS
10 scanner uses the Medipix3 detector chip developed at CERN (Geneva, Switzerland) with charge-
11 summing circuitry to compensate for charge sharing between neighboring detector pixels
12 (Ballabriga *et al.*, 2006).
13
14
15
16
17
18
19
20
21
22
23

24 Interestingly, recent improvements in contrast sensitivity have fueled investigations into the
25 development of novel contrast agents, including NP-based platforms, for preclinical molecular CT
26 imaging (Ashton *et al.*, 2015). As imaging probes, NPs associated with various targeting strategies
27 can facilitate molecular imaging with CT (Ashton *et al.*, 2018). Their ability to package a large
28 payload of imaging moieties enables signal amplification at the target site. Although significant
29 challenges exist due to the low contrast sensitivity of CT relative to nuclear imaging modalities
30 such as PET and SPECT, it is possible to image multiple probes based on different heavy metal
31 (K-edge) materials that are simultaneously present in the body at relatively high spatial resolution.
32
33
34
35
36
37
38
39
40

41 The aim of the current study is to compare preclinical DE-EID and PCD CT for differentiation
42 of NPs based on two elements suitable for K-edge imaging: gadolinium (Gd) and iodine (I). We
43 utilized liposomes, one of the most extensively studied NP platforms, for the fabrication of NP
44 contrast agents. We have developed and extensively studied Liposomal iodine (Lip-I) contrast
45 agents for CT imaging applications in blood-pool, cancer, and cardiovascular imaging (Ghaghada
46 *et al.*, 2016; Starosolski *et al.*, 2015; Annapragada *et al.*, 2012; Badea *et al.*, 2012a). Additionally,
47 we have developed and tested Liposomal Gd (Lip-Gd) contrast agents for MR imaging (Ghaghada
48 *et al.*, 2008). Gadolinium has also been used as contrast material for CT (Gierada and Bae, 1999);
49
50
51
52
53
54
55
56
57
58
59
60

1
2
3 moreover, Gd may have greater potential as a K-edge contrast agent for cadmium telluride (CdTe)-
4 based PCD CT (Muenzel *et al.*, 2017). More importantly, both I and Gd are already used as
5 contrast materials in the clinic, unlike other materials that require extensive toxicity studies before
6 being clinically translated. While some PCD and DE-CT comparison has been attempted at the
7 clinical level (Gutjahr *et al.*, 2016), to our knowledge, this is the first preclinical study to compare
8 *in vivo* DE-EID and PCD CT imaging and to demonstrate the utility of this methodology for cancer
9 imaging.
10
11
12
13
14
15
16
17
18

19 2. MATERIAL AND METHODS

20
21 We begin by introducing the liposomal NP contrast agents used in this work. Short technical
22 descriptions of our dual-source, preclinical DE-EID and PCD CT system setups and our data
23 acquisition are then provided. Based on these details, realistic simulation experiments are
24 conducted to establish limits on the expectations of contrast material decomposition accuracy
25 possible with each system and method. Finally, details are provided for phantom experiments and
26 an *in vivo* micro-CT experiment using a primary mouse model of soft tissue sarcoma.
27
28
29
30
31
32
33
34

35 2.1 Liposomal-based iodine and gadolinium contrast agents for CT

36
37
38 Liposomal-based contrast agents containing I and Gd were fabricated similar to methods
39 described previously (Badea *et al.*, 2012a; Ghaghada *et al.*, 2008; Mukundan *et al.*, 2006). Briefly,
40 a lipid mixture (150 mM) consisting of 1,2-dipalmitoyl-sn-glycero-3-phosphocholine (DPPC),
41 cholesterol, and 1,2-distearoyl-sn-glycero-3-phosphoethanolamine-N-[methoxy (polyethylene
42 glycol)-2000] (DSPE-MPEG 2000) (56:40:4 molar ratio) was dissolved in ethanol. The ethanolic
43 solution was hydrated with either iodixanol solution (550 mg I/ml), for the preparation of Lip-I, or
44 with gadoteridol (500 mM Gd), for the preparation of Lip-Gd. The hydrated solution was
45 sequentially extruded to obtain liposomes of desired size distribution. The resulting solution was
46 diafiltered to remove un-encapsulated iodixanol/gadoteridol. The size distribution of liposomes in
47
48
49
50
51
52
53
54
55
56
57
58
59
60

1
2
3 the final formulation was determined by dynamic light scattering (DLS). The I concentration in the
4 final Lip-I solution was quantified by spectrophotometry ($\lambda = 245$ nm). The Gd concentration in the
5 final Lip-Gd solution was quantified by inductively-coupled plasma atomic emission spectroscopy
6 (ICP-OES). The final I concentration in the Lip-I formulation was 110 ± 4 mg/ml, and the final Gd
7 concentration in the Lip-Gd formulation was 20 ± 3 mg/ml. The average liposome size was $145 \pm$
8
9
10
11
12
13
14
15
16
17
18
19
20
21
22
23
24
25
26
27
28
29
30
31
32
33
34
35
36
37
38
39
40
41
42
43
44
45
46
47
48
49
50
51
52
53
54
55
56
57
58
59
60
6 nm for Lip-I and 219 ± 13 nm for Lip-Gd. The poly-dispersity index for both formulations was less
than 0.15.

2.2 Imaging Systems

2.2.1 DE-EID Micro-CT

Our dual source micro-CT system used for DE-EID micro-CT imaging has been described in detail
previously (Badea *et al.*, 2008). The system incorporates two imaging chains capable of
independently triggered acquisitions. The system contains two G-297 X-ray tubes (Varian Medical
Systems, Palo Alto, CA) with 0.3 mm focal spot size, two Epsilon high-frequency X-ray generators
by EMD Technologies (Quebec, Canada), and two flat-panel CsI based detectors (model Dexela
1512CL, PerkinElmer) with 75 μ m, isotropic pixels. Data acquisition is controlled by an in-house
developed sequencing application written in LabVIEW (National Instruments). The subject is
mounted in a vertical cradle and rotated through all projection angles with a circular scanning
trajectory. The source to detector and source to object distances were 820 and 679 mm for the
first imaging chain and 831 and 680 mm for the second imaging chain. Thus, magnification for the
DE-EID CT system was approximately 1.2.

2.2.2 PCD Micro-CT

Our PCD micro-CT system uses a prototype PCD from DECTRIS AG of Baden-Dättwil,
Switzerland (<https://www.dectris.com/>) model SANTIS 0804 ME based on a 1 mm CdTe sensor
with 150 μ m, isotropic pixels. The PCD has 4 energy thresholds. We use the same type of X-ray
source as for the DE-EID micro-CT system. The subject is mounted in a vertical cradle and rotated

through all projection angles with a circular scanning trajectory. Data acquisition is controlled by an in-house developed sequencing application written in LabVIEW (National Instruments). The source to detector and source to object distances were 831 mm and 680 mm, respectively (a magnification of ~ 1.2). To minimize ring artifacts in our reconstructions, we scanned using a helical trajectory with 3 rotations and vertically translated the object 1.25 cm during scanning. The ring artifacts are caused by pixels with non-linear energy- and time-varying response profiles.

The energy thresholds of the PCD used in this study were set to 25, 34, 50 and 60 keV. We have not subtracted projections between the consecutive energy bins. The first threshold (25 keV) was selected to limit spectral distortions due to charge sharing for low keV photons and to remain well above the detector's noise floor located below 6 keV. The next two thresholds were chosen to image the K-edges of I (33.2 keV) and Gd (50.2 keV). Finally, the last threshold at 60 keV was selected to provide enough counts when imaged with a polychromatic X-ray source at 80 kVp.

2.3 Image Reconstruction

To improve the detectability of low concentrations of I and Gd, both DE-EID and PCD CT data were reconstructed using the iterative spectral CT reconstruction framework we have previously described (Clark and Badea, 2017). Specifically, we applied the split Bregman method with the add-residual-back strategy (Gao *et al.*, 2011) to solve the following optimization problem:

$$X = \underset{X}{\operatorname{argmin}} \frac{1}{2} \sum_e \|RX_e - Y_e\|_2^2 + \lambda \|X\|_{\text{BTV}}, \quad (1)$$

$$\|X\|_{\text{BTV}} := \sum_e \frac{\sum_{i,j} D(i)K(i,j)|W(i)X_e(i,j)|}{\sum_{i,j} D(i)K(i,j)}, \quad (2)$$

$$K(i,j) = \prod_e \exp\left(-\frac{(W(i)X_e(i,j))^2}{2m_e^2\sigma_e^2}\right). \quad (3)$$

This algebraic reconstruction problem solves for the vectorized, reconstructed data, the columns of X , for each sampled threshold (kVp) simultaneously (indexed by e). The reconstruction for each threshold minimizes the reprojection error (R , system projection matrix) relative to the log-

transformed projection data acquired at each threshold (the columns of Y). To reduce noise in the reconstructed results, this data fidelity term is minimized subject to the bilateral total variation (BTV) measured within and between thresholds. Specifically, as shown above, BTV is calculated as the weighted sum of image gradients (intensity gradient operator W), where the weights are computed over a local neighborhood (D domain, index i) and summed over the entire image (index j) and energies. To handle varying noise levels and contrast with energy, range weights (kernel K) are determined by intensity gradient magnitudes relative to the noise level (σ_e) and smoothing parameter (m_e) set for each energy. During iterative reconstruction, BTV is reduced by the application of BF. To maximize redundancy between the reconstructed thresholds and, therefore, minimize noise in the material decomposition results, we employed a specific extension of joint BF known as rank-sparse kernel regression (RSKR). RSKR is similar to the equations above, except that a weighted singular value decomposition is performed across the energy dimension prior to filtration to improve performance and to simplify parameter selection. RSKR and our regularization strength scaling strategy to compensate for different noise level between thresholds are detailed in previous work (Clark and Badea, 2017). All DE-EID and PCD CT phantom and mouse data were reconstructed with the same isotropic voxel size of $123 \mu\text{m}$, facilitating the comparison of results.

2.4 Material Decomposition

For DE-EID micro-CT, material decomposition of Gd and I was performed after reconstruction and Hounsfield units (HU) conversion. Specifically, decomposition used paired reconstructions at two different kVps (E_1, E_2) and solved the following linear system at each voxel:

$$C = A^{-1}b. \quad (4)$$

Expanding the linear system in eq. (4):

$$\begin{bmatrix} C_I \\ C_{Gd} \end{bmatrix} = \begin{bmatrix} CT_{I,E1} & CT_{Gd,E1} \\ CT_{I,E2} & CT_{Gd,E2} \end{bmatrix}^{-1} \begin{bmatrix} CT_{E1} \\ CT_{E2} \end{bmatrix} \quad (5)$$

1
2
3 In this formulation, C is the least-squares solution for the concentration of the I (C_I) and Gd (C_{Gd})
4 in mg/mL in the voxel under consideration. A is a constant sensitivity matrix measured in
5 Hounsfield units per contrast agent concentration (HU/mg/mL) for I ($CT_{I,E1}$, $CT_{I,E2}$) and Gd ($CT_{Gd,E1}$,
6 $CT_{Gd,E2}$) at $E1$ and $E2$, respectively. Finally, b is the intensity of the voxel under consideration at
7 $E1$ (CT_{E1}) and $E2$ (CT_{E2}) in Hounsfield units. After finding the solution to the linear system, non-
8 negativity was enforced by setting voxels with negative concentrations of both materials to zero.
9 Voxels with a negative concentration of one material and a positive concentration of the other
10 material were orthogonally projected onto the subspace of positive concentrations. Values for the
11 coefficients of the sensitivity matrix at each energy ($CT_{I,E1}$, $CT_{I,E2}$, $CT_{Gd,E1}$ and $CT_{Gd,E2}$) were
12 determined empirically using a calibration phantom as described previously (Clark *et al.*, 2013).
13
14
15
16
17
18
19
20
21
22
23
24

25 To decompose spectral PCD micro-CT data, we also used a post-reconstruction
26 decomposition method. Extending the approach of Alvarez and Macovski (Alvarez and Macovski,
27 1976) we performed a basis material decomposition:
28
29
30

$$\mu(E) = a_{PE}\mu_{PE}(E) + a_{CS}\mu_{CS}(E) + a_I\mu_I(E) + a_{Gd}\mu_{Gd}(E). \quad (6)$$

31
32 Given reconstructions acquired with four energy bins, E , the first two terms describe the energy-
33 dependent attenuation, $\mu(E)$, owing to the photoelectric effect (PE) and Compton scattering (CS).
34 The next two terms are basis functions for K-edge materials, in this case I and Gd. For comparison
35 with the DE data, we also performed a PCD DE decomposition in which the 4 energy bins were
36 used to solve the overdetermined system of equations with only two unknowns (i.e. I and Gd
37 concentrations). We call this PCD2, while we use the term PCD4 for 4 basis material
38 decomposition as in eq. (6). After decomposition, the material maps are color coded with I in red,
39 Gd in green, PE in blue, and CS in gray. All colored maps are color merged and displayed in
40 ImageJ (<https://imagej.nih.gov/ij/>).
41
42
43
44
45
46
47
48
49
50
51
52
53
54
55
56
57
58
59
60

2.5 Simulations

To better understand the limits of our preclinical spectral CT imaging methods, we have performed X-ray simulations for both DE-EID and PCD-based imaging using Spektr (Siewerdsen *et al.*, 2004). The energy dependencies of the attenuation for water and I, and Gd solutions are shown in Fig. 1A. Note the K-edges of I (33.2 keV) and Gd (50.2 keV). We have recently reported on both simulations and physical phantom experiments to validate the optimal scanning kVps for DE-CT imaging of the Lip-I and Lip-Gd contrast agents (Badea *et al.*, 2018). The two energy settings that provided maximum contrast discrimination between I and Gd were determined to be 50 kVp with 0.1 mm Cu filtration and 40 kVp without any filtration. Our model included the spectral response of the CsI scintillator. As shown by Fig. 1B, these two X-ray spectral responses are approximately bracketing the K-edge of I at 33.2 keV. We note that with only two EID measurements and with kVps suitable for small animal imaging (i.e. ranging from 40 and 80 kVp), we effectively optimized for only one of the materials (in this case I). CsI (thickness of 0.15 mm) used in the detector's scintillator and the copper filtration are the major determining factors in the increase of I contrast with the 50 kVp spectrum.

Both our simulated and experimental results (Badea *et al.*, 2018) have proved that the above kVp settings provide the best combination with the lowest condition number of the material sensitivity matrix used for material decomposition. The condition number is the ratio of the largest and smallest singular values of a matrix, and it quantifies the potential for error amplification (higher values indicate greater potential for error amplification). All of our *in vivo* and simulated DE-EID projection data was corrected for beam hardening prior to reconstruction. The correction, which improves the linearity of attenuation measurements, was calibrated with an acrylic wedge (Zou *et al.*, 2011).

We have also simulated the spectral response of the PCD micro-CT (see Fig. 1C). The PCD spectral response included the 80 kVp tungsten based X-ray tube spectrum with 0.1 mm Cu

filtration as well as the expected quantum efficiency of detection with 1 mm of CdTe (Radicci *et al.*), but did not model more complex physical phenomena such as charge sharing and pulse pile-up. As shown by Fig. 1C, the PCD spectral response has a peak in close proximity to the K edge of Gd (i.e. 50.2 keV).

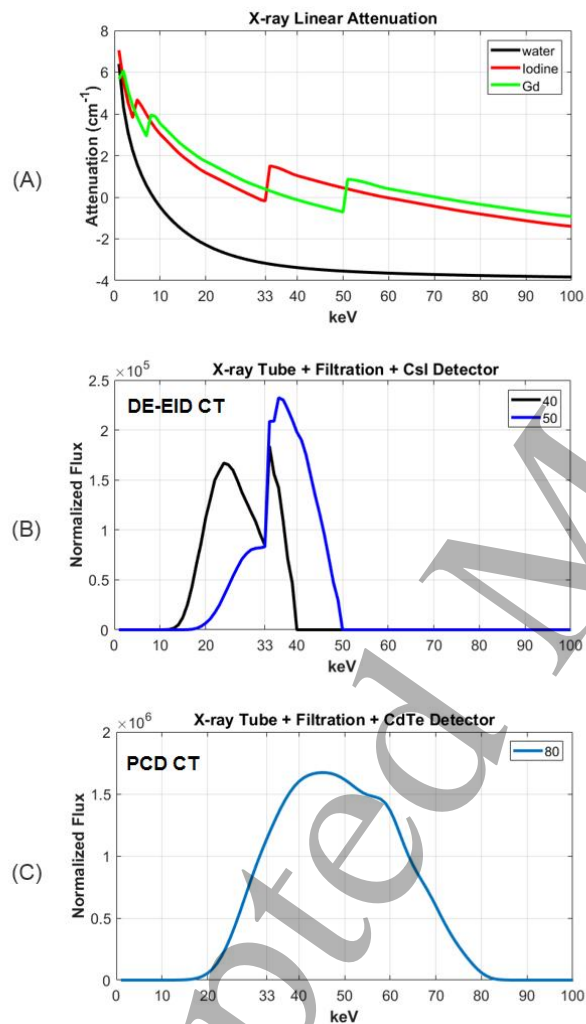


Fig. 1: (A) The attenuation coefficients for water and I and Gd solutions. Note the K-edges of I (33.2 keV) and Gd (50.2 keV). (B) The X-ray spectral response used for DE-EID simulations corresponding to 40 kVp (w/o Cu filtration) and 50 kVp (with Cu filtration). (C) The X-ray spectral response for the PCD CT with the X-ray tube scanning with 80 kVp and Cu filtration.

The DE-EID and PCD-based spectral responses were used in the x-ray imaging forward models to create realistic projections from a digital phantom. We have previously introduced the

1
2
3 digital contrast and resolution phantom, which was originally constructed to assess the fidelity of
4 hybrid spectral CT reconstruction (Clark and Badea, 2017). The phantom consists of a cylinder of
5 water with a diameter of 4.5 cm, scaled to match the diameter of the cradle used for scanning adult
6 mice. The cylinder is divided into three segments (disks) along the z-axis. As shown in Fig. 2, each
7 disk is dominated by a single contrast material we aim to separate *in vivo*: I (red), calcium (blue),
8 and Gd (green). The materials are present in realistic concentrations for small animal micro-CT—
9 10 mg/ml of I, 75 mg/ml of calcium, and 10 mg/ml of Gd in water (material fraction = 1.0). To
10 provide a visual assessment of spatial resolution, each disk contains a set of line pairs which
11 discretely represent spatial frequencies from 1 to 4.07 line pairs per mm (lp/mm). To assess the
12 trade-offs in feature detection with feature size and material concentration, a grid of spheres is
13 included within each disk. Along the vertical axis, the diameters of these spheres vary from 1.0
14 mm to 2.5 mm in increments of 0.5 mm, with some truncation due to discretization. Along the
15 horizontal axis, the concentrations of each disk's material take on the following fractions of the
16 maximum concentration: 1.0, 0.5, 0.25, and 0.1. Additional vials (3.5 mm cylinders) of I, calcium,
17 Gd, and water (invisible) are included below the spheres (material fraction = 0.5) and were used
18 for material sensitivity measurements.
19
20
21
22
23
24
25
26
27
28
29
30
31
32
33
34
35
36

37 Additional steps were taken to better match the image noise of the *experimental*
38 *acquisitions*. Specifically, photon counts were adjusted such that when the recorded counts were
39 drawn from a Poisson distribution with a mean equal to the attenuated intensity, the resultant
40 filtered backprojection (FBP) reconstructions reproduced the expected noise standard deviations
41 measured in water. Reference water noise measurements were taken at the center of the physical
42 calibration phantom and were matched to the water vial of the digital phantom. For the DE-EID
43 simulations in the 40 kVp scan, we used $1e4$ photons / line integral to match a noise standard
44 deviation of 83 HU; in case of the other scan at 50 kVp + Cu filtration, we used $4.5e3$ photons /
45 line integral to match a noise level of 122.5 HU. For the PCD simulations involving a scan at 80
46
47
48
49
50
51
52
53
54
55
56
57
58
59
60

1
2
3 kVp with Cu filtration, we used 1.25×10^4 photons / line integral, which resulted in noise levels of
4
5 91,124, 237, and 416 HU for the 4 energy thresholds (25, 34, 50 and 60 keV).
6

7 To better model the limited energy resolution of the PCD, we used a Gaussian energy spread
8
9 function with a standard deviation of 2.5 keV to model non-ideal spectral binning. While simplified,
10
11 Gaussian smoothing of the spectral binning functions is consistent with previous experimental
12
13 measurements of monoenergetic energy-spread functions in CdTe-based PCDs (Schlomka *et al.*,
14
15 2008; Clark *et al.*, 2015). Furthermore, a standard deviation of 2.5 keV reproduced the empirically
16
17 measured condition number of the material sensitivity matrix for the real PCD system (four
18
19 materials). Notably, all condition numbers were measured following unit normalization of the
20
21 sensitivity vectors for each material. In the case of DE-EID, the simulated and measured condition
22
23 numbers were close: 5.5 in simulations and 4.9 for the experimental scans. The condition number
24
25 for the PCD4 was 34 in simulations and 37.9 for the experimental scans. By comparison, the
26
27 condition number in the PCD2 decomposition was 5.58 in simulations and 6.5 in the experimental
28
29 scans.
30
31
32
33

34 2.6. Quantitative Evaluation

35
36
37 Several metrics were used to quantitatively evaluate the results of DE-EID and PCD material
38
39 decomposition using the digital phantom. *Root mean square error* (RMSE) assessed the accuracy
40
41 of the I and Gd maps and was computed as follows:
42

$$43 \text{ RMSE} = \sqrt{\frac{1}{n} \sum_{y=1}^n ([C]_y - [C]_0)^2}, \quad (7)$$

44
45 where y indexed the voxels, n was the total number of voxels, $[C]_y$ was the measured concentration
46
47 of $C = \text{I}$ or $C = \text{Gd}$ in voxel y , and $[C]_0$ was the expected concentration of I or Gd in voxel y .
48

49
50
51 *Contrast to noise ratio* (CNR) characterized the detectability of each element within the
52
53 decomposition maps afforded by the different scans and was computed for I and Gd as follows:
54
55
56
57
58
59
60

$$\text{CNR} = \frac{|m_y - m_b|}{\sqrt{\sigma_y^2 + \sigma_b^2}}, \quad (8)$$

where m_y and σ_y^2 refer to the mean and variance measured for one of the two materials (i.e. I or Gd) and m_b and σ_b^2 refer to the mean and variance measured in a background region of interest (the water vial of the phantom). To assess the limits of detectability, the Rose criterion was applied stating that a given concentration of I or Gd could be reliably detected when the CNR was ≥ 5 (Rose, 1948).

2.7 Phantom Experiments

Physical phantom experiments were designed and performed to validate the simulations. First, we used vials of water, I, and Gd to verify that the PCD threshold positions yielded the expected changes in contrast around the K edges of I and Gd. These projections were log transformed and normalized to the attenuation of water to make the K-edge associated contrast enhancements more distinct.

Next, a 3D printed phantom containing solutions of I in water (9.25, 5.3, 3.75, and 2 mg/ml) and Gd in water (10.5 and 2.5 mg/ml) was scanned. The DE-EID CT scan used 40 kVp, 50 mA, and 25 ms for one x-ray tube and 50 kVp with Cu (0.1 mm) filtering, 80 mA, and 12.5 ms exposures for the second x-ray tube. A delay of 100 ms was kept between the exposures of the two x-ray tubes to avoid cross-scatter. A total of 720 projections for each energy were acquired over a single 360° rotation. As previously mentioned, the DE-EID projection data was corrected for beam hardening prior to reconstruction. For the PCD CT scans, we used 80 KVp (with 0.1 mm Cu filtering), 2 mA, 200 ms/exposure with 900 projections acquired over a 1.25 cm vertical translation and three full rotations (helical acquisition, pitch = 1.1). The radiation dose was 162 mGy for DE-EID and 43 mGy for PCD CT. Thus, the radiation dose comparison between the two imaging

procedures shows that the PCD scanning was achieved with ~3.8 times less radiation dose compared to DE-EID CT.

2.8 In Vivo Experiments

In vivo experiments were conducted in accordance with the governing protocol approved by the Institutional Animal Care and Use Committee of Duke University Medical Center (protocol A251-14-10). A CT imaging-based biodistribution study was performed for Lip-Gd and Lip-I in C57BL/6 mice (n=6). Three mice were intravenously administered with Lip-I (1.32 mg I/kg) and other three mice with Lip-Gd (0.4 mg Gd/kg). Whole body CT imaging was performed at 0, 1, 2, and 3 days post-injection using EID-CT to quantify the concentrations Lip-I or Lip-Gd in the blood, liver, spleen, kidneys, and muscle.

For the tumor imaging study, we used a carcinogen-induced and genetically engineered primary model of soft tissue sarcoma developed in $p53^{fl/fl}$ mice. Primary sarcoma lesions were generated in the hind limb by intramuscular delivery of adenovirus expressing Cre recombinase (Kirsch *et al.*, 2007), followed by injection of 300 μ g 3-methylcholanthrene (Sigma). Tumors resembling human undifferentiated pleomorphic sarcoma developed approximately 8-12 weeks after injection. Imaging studies were initiated when tumors were palpable (>100mg), continuing through various stages of disease progression. Three mice were intravenously administered Lip-Gd contrast agent (0.4 mg Gd/kg body weight) and imaged 3 hours later with both DE-EID and PCD micro-CT (Day 0). Three days later (Day 3), the same animals were injected with Lip-I (1.32 mg I/kg body weight) and re-imaged. The dose (mg/kg) of I and Gd contrast agents used for our *in vivo* studies are within the range of doses that we and others have used extensively in pre-clinical studies for tumor (Ghaghada *et al.*, 2011) (Badea *et al.*, 2012a) and cardiovascular imaging (Ashton *et al.*, 2014; Lee *et al.*, 2014). These dose levels have not posed safety concerns and therefore are acceptable for pre-clinical studies. Material decomposition maps were computed and analyzed for *in vivo* separation and quantification of I and Gd concentrations.

The I and Gd maps resulting from the decomposition at Day 3 were used to compute two metrics for functional characterization of tumor vasculature—fractional blood volume (FBV) using Lip-I and tumor accumulated mass of nanoparticles using Lip-Gd as previously described (Clark *et al.*, 2013). FBV, which is analogous to micro-vessel density (MVD) and an indicator of tumor perfusion was computed on a whole tumor basis as follows:

$$C'_n = \begin{cases} 0, & C_n \leq C_b \\ C_n, & C_n > C_b \end{cases}$$

$$FBV = \frac{1}{N * C_{Max}} * \sum_{n=1}^N C'_n$$

where C_b was the threshold of detectability for Lip-I determined by measurements in the muscle of the non-tumor leg, C_n and C'_n were the concentrations in voxel n before and after thresholding with C_b , N was the total number of tumor voxels, and where C_{Max} was the blood pool concentration of iodine measured in the lumen of the descending aorta.

Accumulated mass (AM), an indicator of tumor 'leakiness' or enhanced permeation and retention (EPR) status (Maeda, 2001), measured the accumulation of Lip-Gd within tumor and was computed as follows:

$$C'_n = \begin{cases} 0, & C_n \leq C_b \\ C_n, & C_n > C_b \end{cases}$$

$$AM = v * \sum_{n=1}^N C'_n$$

Where, C_n and C'_n were the concentrations in voxel n before and after thresholding with C_b measured as described above, and v was the volume of a single voxel.

3. RESULTS

The simulation results for our digital phantom with its I, calcium, and Gd sections are shown by Fig. 2. We compare decomposition results for DE-EID, PCD2 (2 materials I, Gd), and PCD4 (4 materials: PE, CS, I, and Gd) decompositions. Since the DE decompositions account for only two materials (I and Gd), the calcium (corresponding to bone) mapping is incorrect (for DE-EID, calcium appears mapped as Gd and for PCD-DE, as I). This is because of an implicit assumption required for our DE decomposition of two contrast agents, namely that all positively enhancing voxels (>0 HU) are composed of I and Gd. Notably, beam-hardening correction reduced the appearance of Gd artifacts around the periphery of the phantom (only corrected results shown). Since the PCD acquisition was performed at 80 kVp with Cu filtration, the lower part of the spectrum is filtered out. Furthermore, the PCD acquisition excludes photons with a recorded energy less than 25 keV. Thus, the PCD2 and PCD4 decompositions exhibit minimal beam hardening artifacts. Since the PCD4 decomposition is a fundamental decomposition (i.e. it should be able to represent all present materials exactly), it robustly maps all material vials to their expected material maps, including the representation of calcium within the PE map. Note that the spheres in the column with the lowest concentrations of I and Gd (1 mg/ml) cannot be reliably distinguished in PCD4 decomposition. Fig. 2 also shows I and Gd RMSE values in the lower-left corners of each decomposition. We observe that I and Gd decompositions are similarly accurate for all methods, with a small advantage for the DE-EID decomposition.

Fig. 3 presents CNR comparisons for the same simulation results. According to the Rose criterion ($\text{CNR} > 5$), DE-EID and PCD based acquisitions were able to detect both I and Gd at 10 and 5 mg/ml concentrations. However, 2.5 mg/ml of I was only detectable with the DE-EID acquisition.

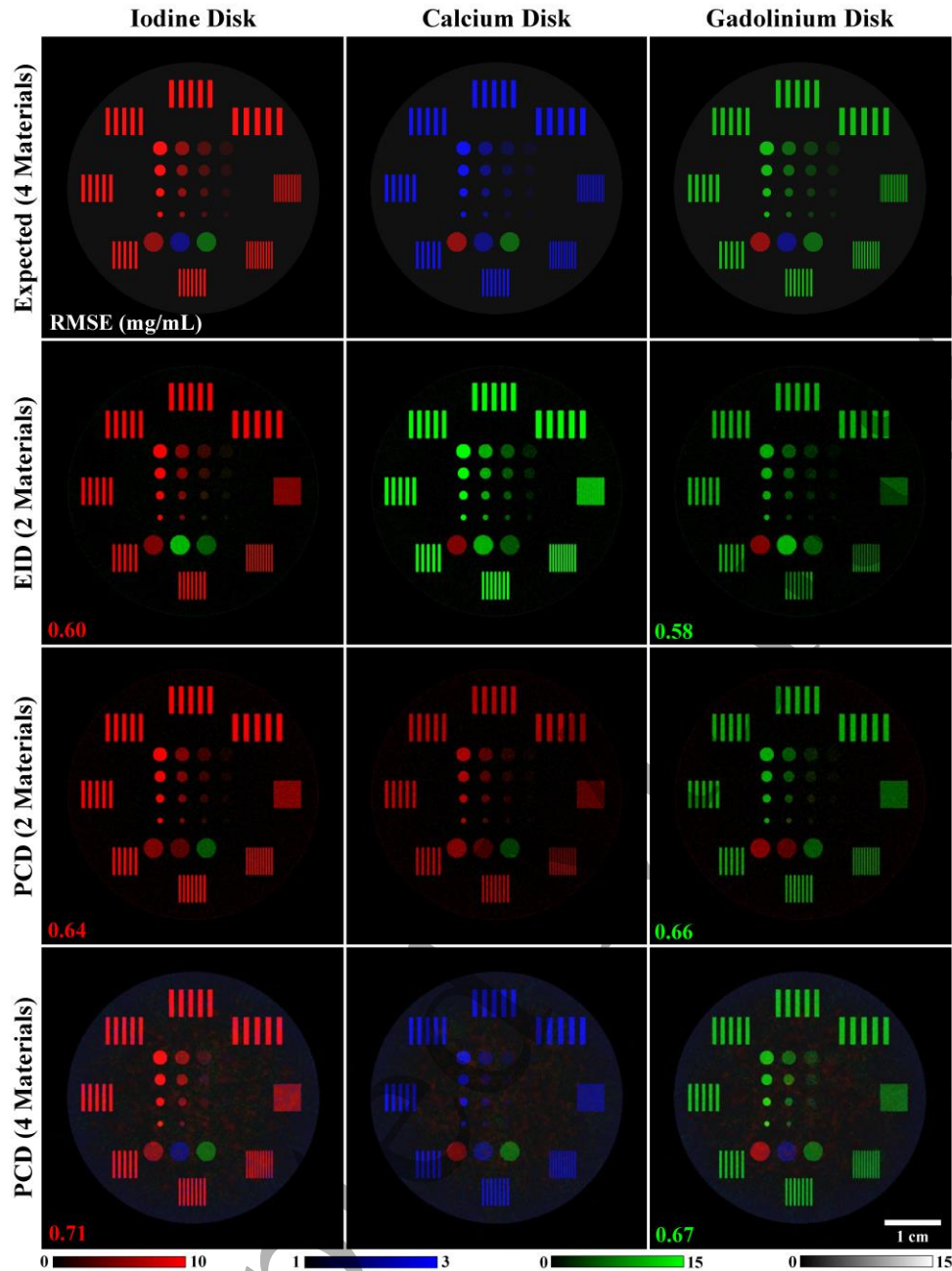


Fig. 2: Tomographic axial slices through the digital phantom (top row) with the expected material maps through the disks containing I, calcium, and Gd. The following three rows show results for material decompositions corresponding to the DE-EID, PCD2, and PCD4 cases. The I is shown in red, calcium (PE) in blue, Gd in green, and CS in gray. RMSE values computed relative to the expected values (over 50, 2D slices) are shown in the lower corner of the I and Gd images. Concentration (water fraction) windowing for each material map is shown at the bottom of the figure.

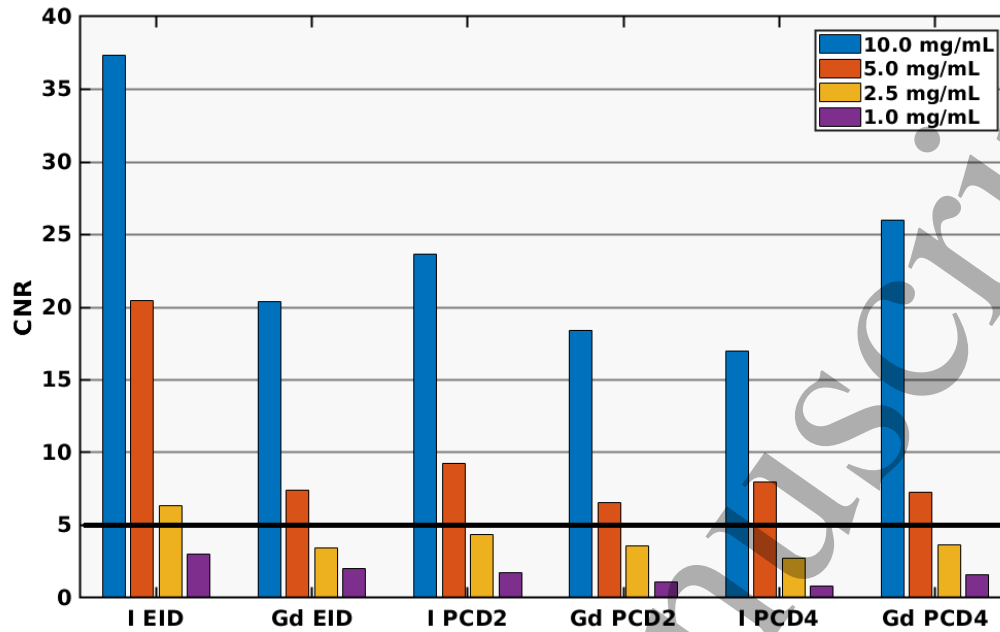


Fig. 3: Comparison of CNRs measured in the simulation studies, with concentrations per column and with CNR values averaged over all four spheres. CNRs are shown for I and Gd in the DE-EID, PCD2 (two material decomposition), and PCD4 (four material decomposition) cases. The solid horizontal line indicates CNR=5, which was used for determining minimal detectable concentrations (Rose, 1948).

Fig. 4 presents the projection-based experimental validation of the threshold settings of the PCD. We measured a 51% increase in contrast for Gd at 50 keV relative to 34 keV; similarly, the contrast increase for I was 20% at ~34 keV relative to 25 keV. Our simple experiment confirms that the setting of the thresholds is correct.

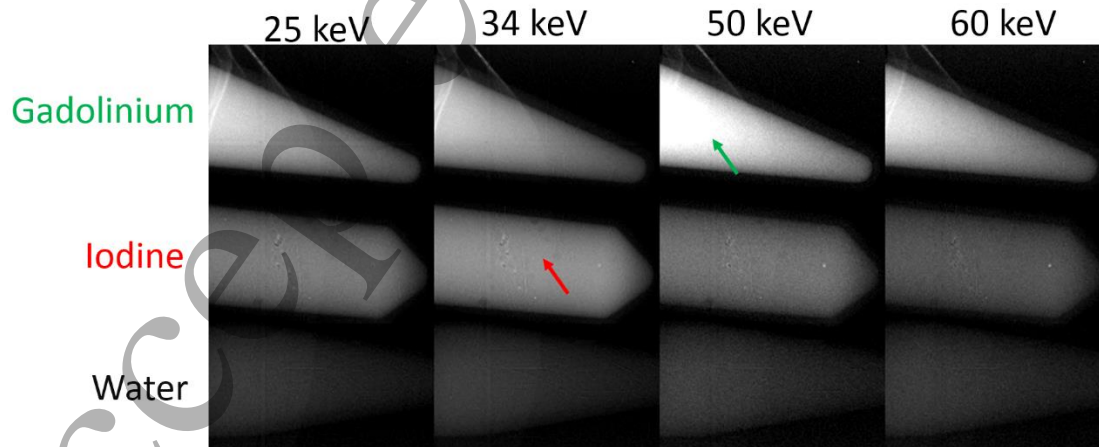


Fig. 4: Experimental validation of the PCD thresholds in a phantom containing vials with I and Gd solutions in water. Projections are compared following water normalization. There is a clear increase in contrast for Gd at ~50 keV. The contrast enhancement of I is less prominent at ~34 keV. These projections were not subtracted between the consecutive energy thresholds.

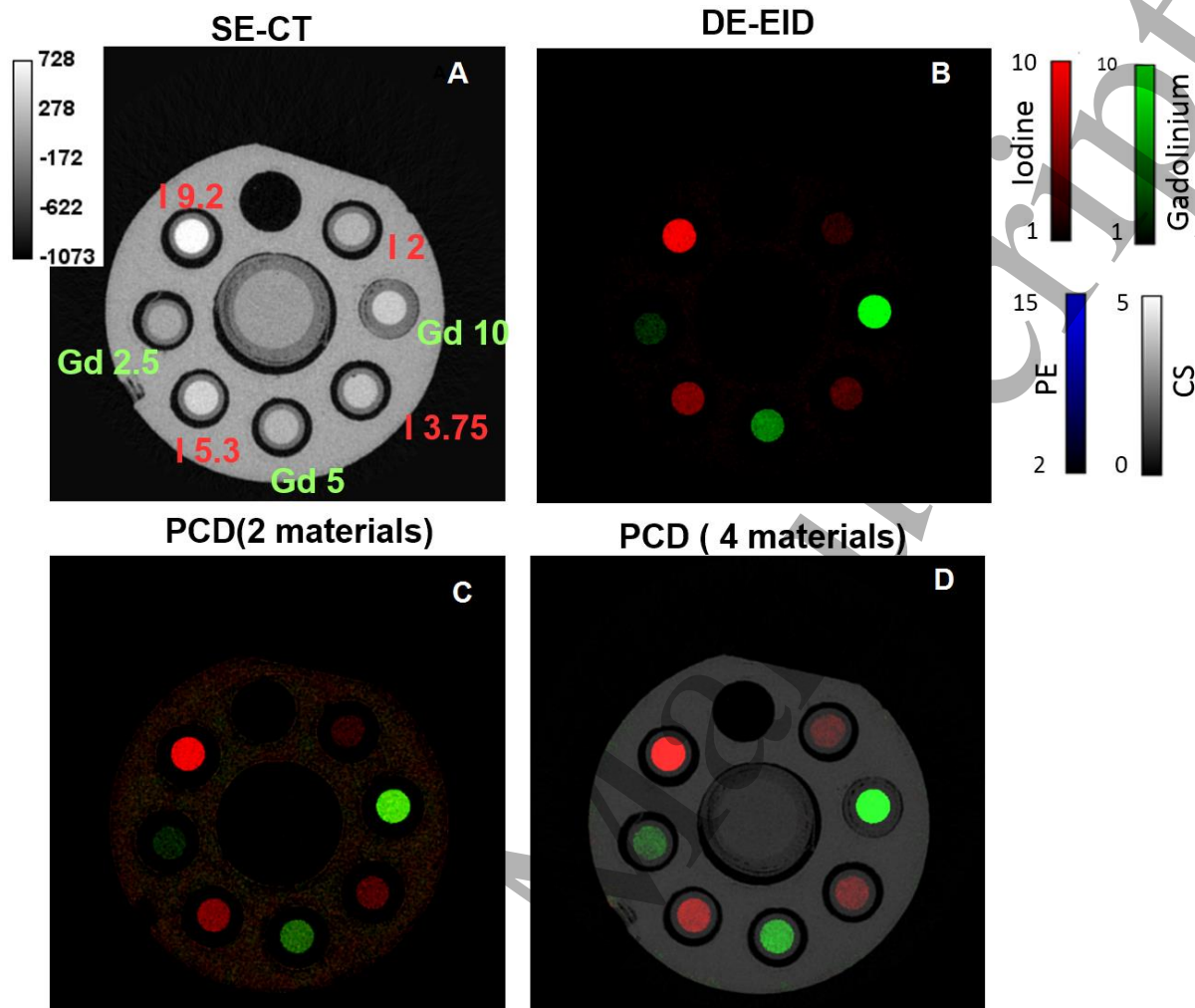


Fig. 5: The phantom (A) and the material decomposition maps for DE-EID(B) PCD (2 materials) (C) and PCD 4 materials (D). I vials appear in red and Gd vials appear in green.

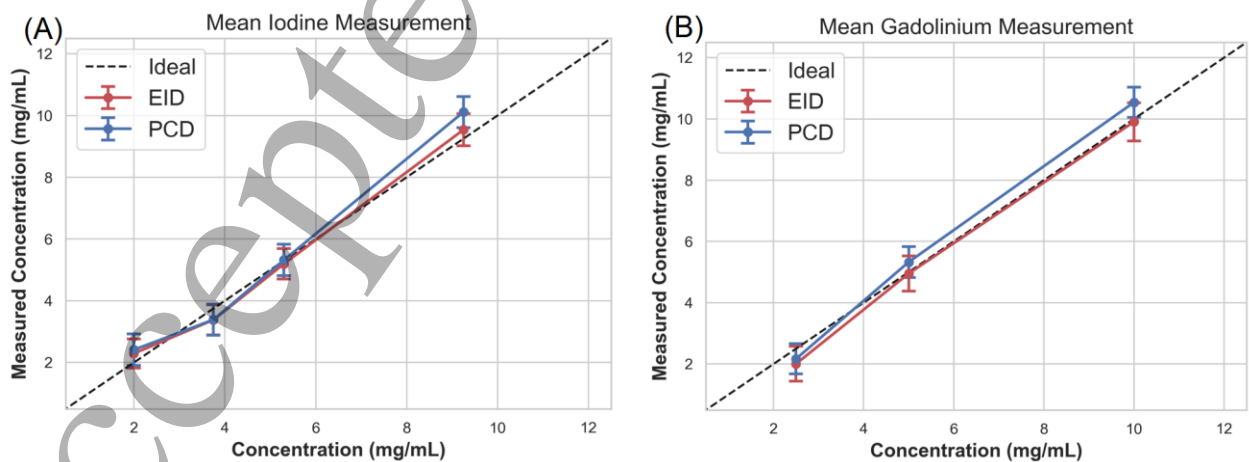


Fig. 6: The plots of measured versus true concentrations for all vials in the phantom containing I (A) and Gd (B) for DE-EID and PCD (4 materials) CT. The bars represent standard deviations of the measured concentrations.

1
2
3
4
5 In Figs. 5 and 6 we present the results of the physical phantom experiments and compare
6 material decomposition results for DE-EID and PCD scans. In general, all vials containing I and
7 Gd are visible and correctly identified in terms of material for all decompositions. As indicated
8 earlier, the condition numbers for the normalized sensitivity matrices were 4.9 for DE-EID and 37.9
9 for PCD4, suggesting a more difficult problem and potentially higher noise amplification for PCD
10 spectral decomposition.
11
12
13
14
15
16
17

18 The 3D printed PLA phantom appears in the PCD2 decomposition as a small constant bias
19 in the I map. This is due to the fact that PLA is denser than water (HU value >0), resulting in
20 apparent positive concentrations of contrast material, similar to calcium in the simulation
21 experiments. A similar small constant bias appears in the DE-EID but on the Gd map. Finally,
22 PCD-based decomposition to 4 material maps (I, Gd, PE, and CS) appears to provide a good
23 visual representation of the phantom. We focus next on a comparison of DE-EID and PCD4 results.
24 The RMSE of I was 0.26 mg/ml in the DE-EID and 0.46 mg/ml in the PCD decompositions. For
25 Gd, the RMSE was 0.25 mg/ml for DE-EID and 0.37 mg/ml for the PCD decompositions. Thus,
26 similar to the simulation results, DE-EID CT provided slightly more accurate I and Gd
27 decompositions. This is also apparent in the plots of measured vs true concentrations presented
28 in Fig.6. Analysis of CNR in material maps indicates better performance for DE-EID decomposition
29 compared to PCD decomposition. For example, CNR computed for the 2 mg/ml I vial was 10.65
30 for DE-EID CT and 8.4 for PCD CT; similarly, the 2.5 mg/ml Gd vial had a CNR of 8.01 for DE-EID
31 CT and 7.72 for PCD CT. This finding is not surprising since the PCD decomposition had a
32 significantly higher condition number compared to the DE-EID decomposition. Moreover, by setting
33 the threshold at 25 keV we have rejected some of the photons arriving at the PCD detector, which
34 may be also a reason for the reduced CNR. Note that the experimental CNR values appear to be
35 slightly better than in our simulations, and according to Rose criterion, are detectable. This is likely
36
37
38
39
40
41
42
43
44
45
46
47
48
49
50
51
52
53
54
55
56
57
58
59
60

because the simulation CNR values were measured within and averaged over spheres of small diameter (1.0-2.5 mm), while these physical phantom measurements were taken in larger vials.

The biodistribution study in six C57BL/6 mice showed uptake and systemic clearance routes for Lip-I and Lip-Gd, consistent with our previously published results (Fig. 7) (Mukundan *et al.*, 2006). The liposomal contrast agents demonstrated the classical NP biodistribution profile: long circulating blood-pool characteristics with clearance primarily via the organs of the reticulo-endothelial system, namely the liver and spleen. The blood half-lives assuming a first order clearance rate constant, were approximately 46.5 hours for Lip-I and 48 hours for Lip-Gd.

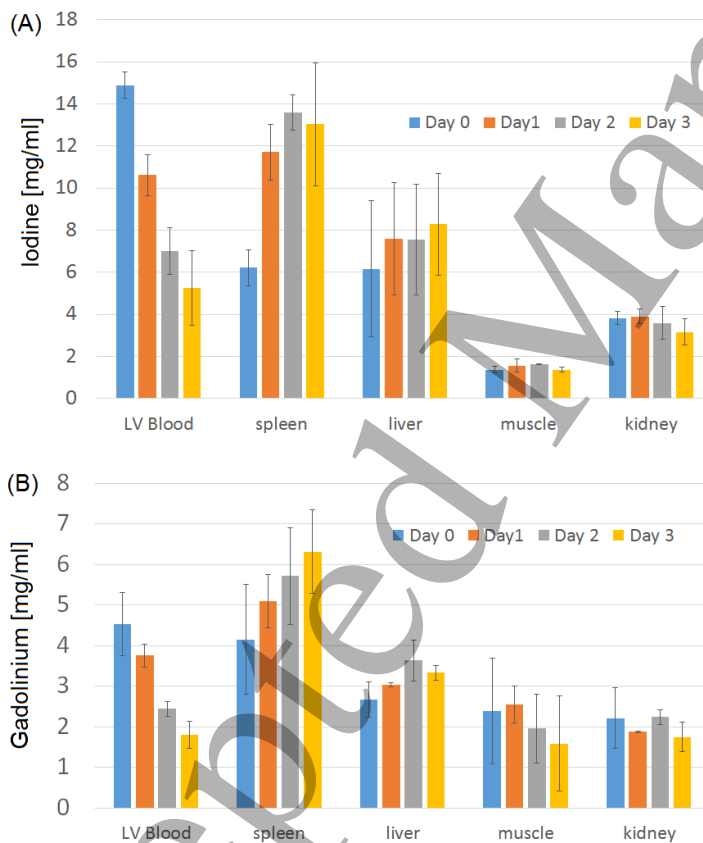


Fig. 7: The biodistribution of Lip-I (A) and Lip-Gd (B) illustrated in the plots of the mean values for the uptake of Lip-I (n=3 mice) and Lip-Gd (n=3 mice) in blood and target organs over 4 days. The error bars represent the standard deviation of concentrations.

Fig. 8 shows examples from our *in vivo* tumor imaging experiments at Day 3 and compares reconstructed DE-EID and PCD CT axial slices and their corresponding material decompositions.

Note that our reconstruction achieves low levels of noise while maintaining contrast characteristics for different energies. Material decomposition results for the sarcoma tumor imaging experiments are also shown for DE-EID CT (Fig. 9) and PCD CT (Fig. 10) at Day 0, containing only Lip-Gd, and Day 3, containing both Lip-Gd and Lip-I contrast agents. To better visualize the continuity of structures, we present maximum intensity projections (MIPs) over a volume in both axial and coronal orientations.

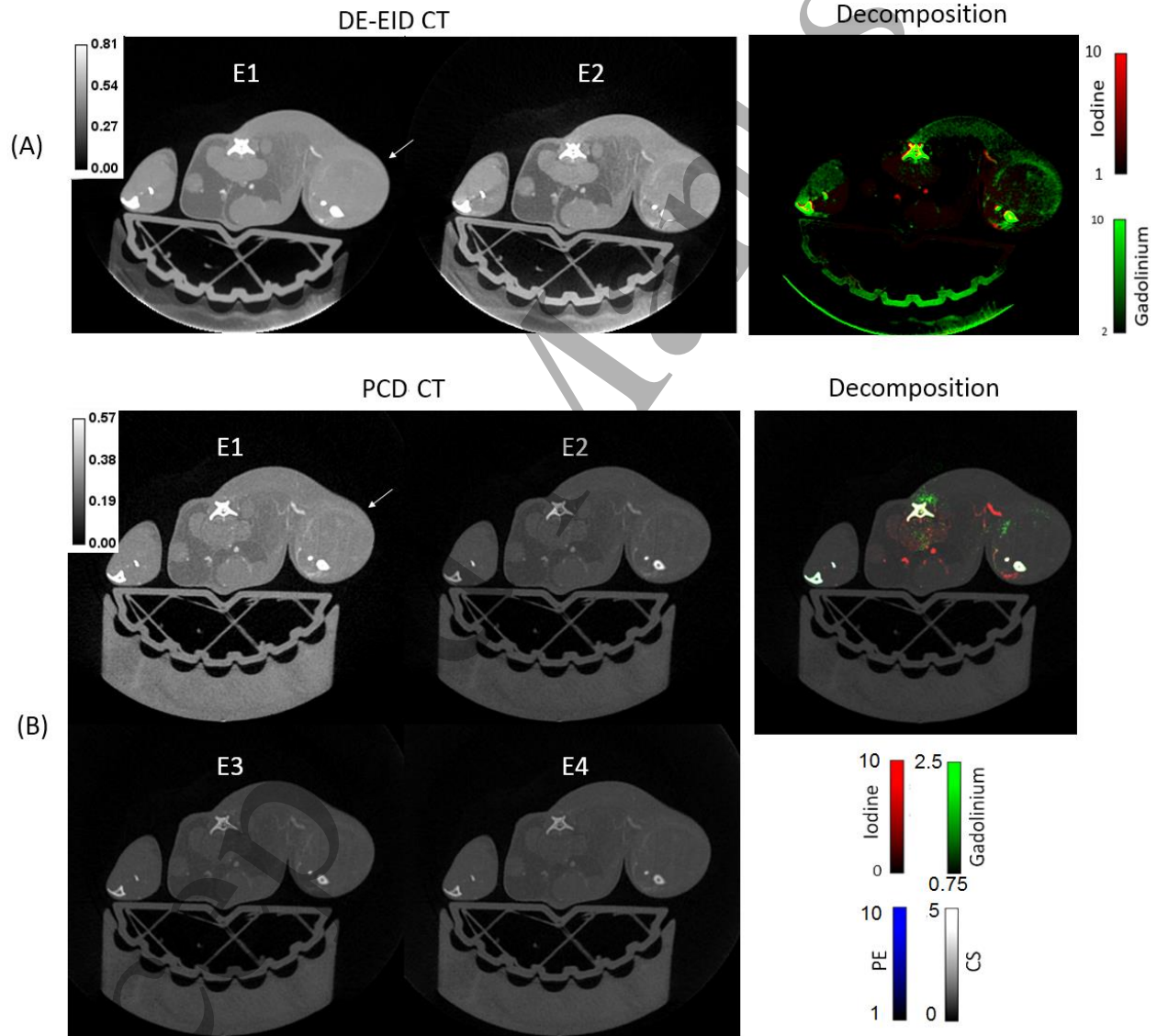


Fig. 8. Examples of DE-EID CT (A) and PCD CT (B) axial reconstructed slices at different energies and their material decomposition maps at Day 3. The sarcoma tumor is positioned on the leg and is indicated by white arrows. The values in the color bars are in [1/cm] for the reconstructed images and in [mg/ml] (I, Gd) and [water fraction] (PE, CS) for the material decompositions.

At Day 3 (3 days after administration of Lip-Gd), Lip-Gd is cleared from the vascular compartment and accumulates in the liver and spleen due to its systemic clearance via these organs. Additionally, the NP contrast agent accumulates in the sarcoma tumor due to the enhanced permeability and retention (EPR) effect (Maeda, 2001). However, Lip-I is expected to be in the vascular compartment since imaging was performed shortly after administration of the agent, enabling the visualization of blood vessels. At Day 0, just after the Lip-Gd injection, the Lip-Gd concentration in the blood, determined from PCD CT, was 4.28 mg/ml. We note vascular enhancement in the tumor. At Day 3, both vasculature (via the I map, shown in red) and tumor EPR via Lip-Gd accumulation (green) are clearly visible.

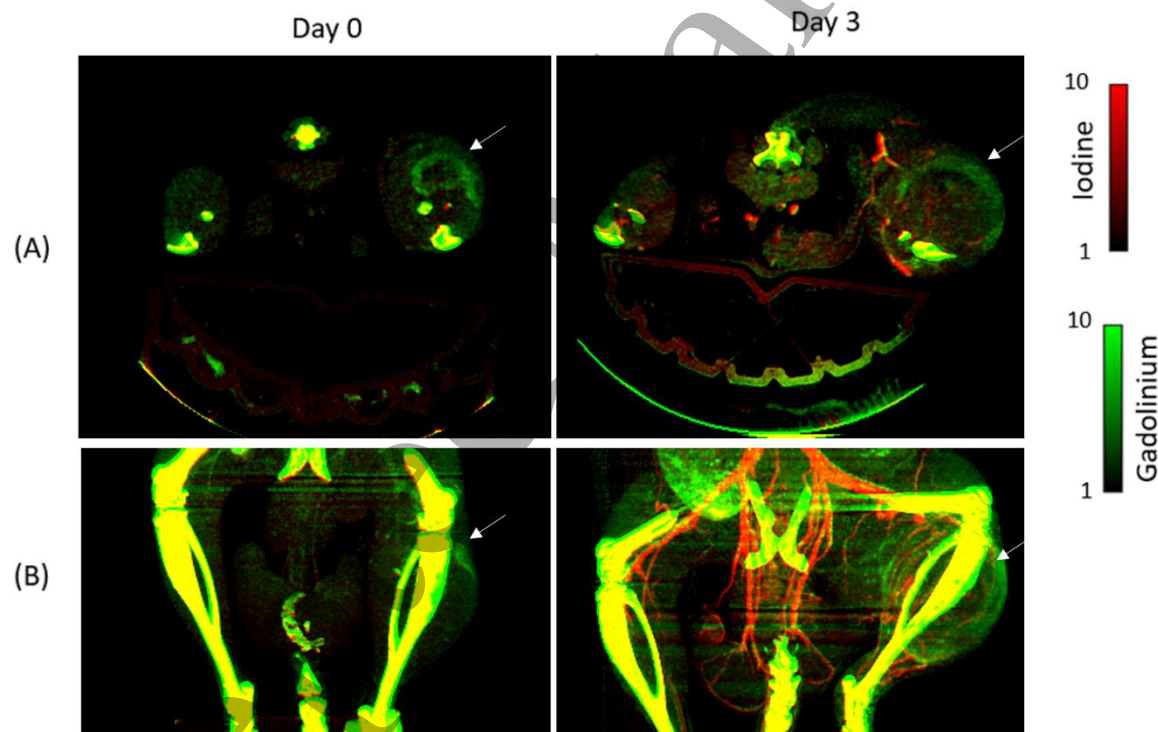
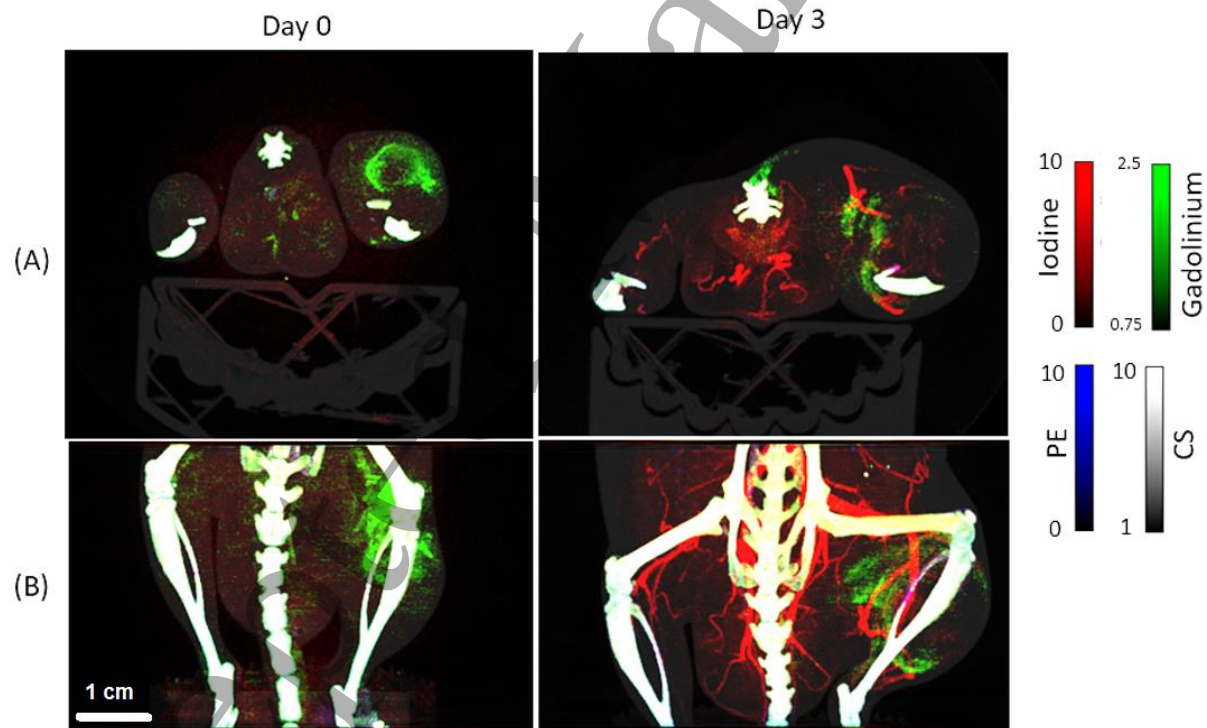


Fig. 9: MIPs based on DE-EID CT decompositions of a mouse with a sarcoma tumor (white arrows) in axial (A) and coronal (B) orientations at Day 0 and Day 3.

The DE-EID results in Figs. 8 and 9 show post-image processing errors around the structure edges (such as bones) caused by small imperfections in registration between the two energy scans. Furthermore, the mouse soft tissue appears to contain some Gd background as a

1
2
3 result of the only two materials decomposition. PCD results shown in Figs. 8 and 10 appear to be
4 superior in quality to DE-EID results, with a cleaner soft tissue background and without artifacts
5 caused by registration imperfections, since all four energy maps are acquired at the same time
6 and with the same geometry. PCD-CT was able to clearly separate Gd signal (EPR-based tumor
7 accumulation) from I signal (vascular compartment). Furthermore, the ability to decompose PE
8 and CS maps enables the separation of bone from contrast material. In Fig.11, we compare MIPs
9 based on material decompositions from DE-EID and PCD-CT in two additional sarcoma-bearing
10 mice imaged at Day 0 and Day 3. Functional metrics of tumor vasculature i.e., FBV measured
11 using Lip-I and AM using Lip-Gd, were determined at Day 3 for both DE-EID and PCD-CT. Note
12 that the two modalities provide similar values for these measures.
13
14
15
16
17
18
19
20
21
22
23
24



49 **Fig. 10:** MIPs based on PCD CT decompositions of a mouse with a sarcoma tumor in axial (A) and coronal
50 (B) orientations at Day 0 and Day 3.
51
52
53
54
55
56
57
58
59
60

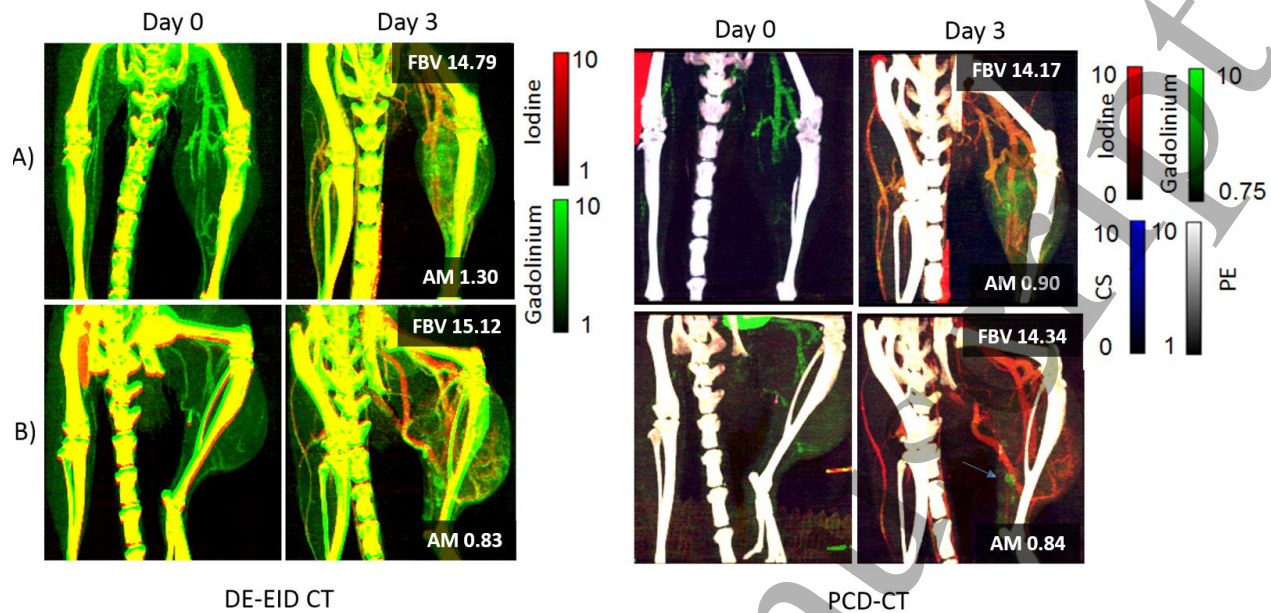


Fig. 11: MIP decomposition comparison in two different mice (A) and (B) for Day 0 and Day 3 with DE-EID (left) and PCD-CT (right). For each mouse, fractional blood volume (FBV) and accumulated mass (AM) were computed using Lip-I and Lip-Gd, respectively at Day 3.

4. DISCUSSION AND CONCLUSIONS

Micro-CT imaging plays a major role in the preclinical study of clinically-relevant pathologies. Advances in preclinical CT contrast agents have expanded the role of micro-CT from anatomic imaging to interrogating the role of vasculature in various disease models. The advent of spectral capabilities in micro-CT have further empowered the modality to extract *in vivo* functional and quantitative information about disease progression and treatment response using multiple contrast agents for simultaneous physiological and molecular imaging. Additionally, the quantitative nature of the modality facilitates conduct of preclinical studies with a strong potential for clinical translation.

In this work, we compared two spectral micro-CT imaging methods for *in vivo* preclinical cancer imaging: DE-EID and PCD-based micro-CT using NPs based on I and Gd. Overall, PCD CT with a fundamental decomposition into PE, CS, I, and Gd provided lower background signal, was not significantly affected by beam hardening, and eliminated any potential for misregistration artifacts between energies, providing cleaner *in vivo* decomposition results in spite of a higher

1
2
3 condition number. However, we acknowledge that the DE-EID results can be improved by
4 improving registration between imaging chains and reducing calcium blooming via model-based
5 reconstruction. Such corrections are under investigation.
6
7
8
9

10 A limitation of the present study is that the radiation dose was not the same for the DE-EID
11 and PCD scans for an objective comparison. However, according to the Rose criterion ($CNR > 5$)
12 applied to the experimental results (see Fig. 5), the detectability limits were approximately 2.5
13 mg/ml for both DE-EID CT and PCD CT, even if the radiation dose was approximately 3.8 times
14 lower with PCD CT.
15
16
17
18
19
20

21 Although we have demonstrated visualization of Gd with a NP formulation containing ~5.5
22 times lower Gd concentration (20 mg/ml) compared to I (110 mg/ml), higher Gd concentration
23 would be beneficial for spectral CT imaging. Notably, iterative reconstruction was extremely
24 beneficial in providing low noise reconstruction results for improved low concentration detectability
25 of Gd, and was applied equivalently to both the EID and PCD data.
26
27
28
29
30
31

32 Our spectral imaging methods could be useful for non-invasive, simultaneous visualization
33 of multiple *in vivo* targets as well as to study the *in vivo* fate and distribution of multiple NPs.
34 Furthermore, the ability to spectrally separate contrast agent elements (I, Gd) from calcium would
35 be useful for molecular imaging and quantifying delivery of NPs in bone pathologies. The accuracy
36 and sensitivity limits of this method are being explored together with more sophisticated spectral
37 reconstruction methods. In the long term, preclinical spectral CT systems such as ours could serve
38 for developing NPs that show promise in the field of cancer theranostics (therapy and diagnostics).
39 Liposome formulations similar to Lip-I and Lip-Gd are also used to deliver chemotherapy (e.g.
40 Doxil). As shown by Fig.11, spectral CT can be used to simultaneously and quantitatively evaluate
41 functional metrics of tumor vasculature i.e., tumor's fractional blood volume (FBV) and tumor
42 'leakiness' determined by measuring accumulated mass (AM) of nanoparticle contrast agent. The
43 measurement of accumulated mass using Lip-Gd also serves as a surrogate for quantifying
44
45
46
47
48
49
50
51
52
53
54
55
56
57
58
59
60

intratumoral distribution patterns of liposomal chemotherapeutics. By being fast, cost-effective, and widespread, spectral micro-CT offers the ideal imaging method for theranostics probes based on high-Z, K-edge materials.

Acknowledgements

All work was performed at the Duke Center for In Vivo Microscopy and was supported by the NIH National Cancer Institute (R01 CA196667, U24 CA220245). Support was also provided by an NIH training Grant, T32-EB001040. This work was made possible by the loan of a SANTIS 0804 ME photon counting x-ray detector prototype from DECTRIS AG of Baden-Dättwil, Switzerland (<https://www.dectris.com/>). Special thanks to Drs. Spyridon Gkoumas and Thomas Thuring for the installation of the photon counting x-ray detector prototype and for technical support. We would also like to acknowledge Dr. David Kirsch for providing mice and Dr. Yi Qi for help with the animal experiments.

References

- Alvarez R E and Macovski A 1976 Energy-selective reconstructions in X-ray computerized tomography *Physics in medicine and biology* **21** 733-44
- Anderson N, Butler A, Scott N, Cook N, Butzer J, Schleich N, Firsching M, Grasset R, De Ruiter N and Campbell M 2010 Spectroscopic (multi-energy) CT distinguishes iodine and barium contrast material in MICE *European Radiology* **20** 2126-34
- Annapragada A V, Hoffman E, Divekar A, Karathanasis E and Ghaghada K B 2012 High-resolution CT vascular imaging using blood pool contrast agents *Methodist DeBakey Cardiovasc J* **8** 18-22
- Ashton J R, Befera N, Clark D, Qi Y, Mao L, Rockman H A, Johnson G A and Badea C T 2014 Anatomical and functional imaging of myocardial infarction in mice using micro-CT and eXIA 160 contrast agent *Contrast Media Mol Imaging* **9** 161-8
- Ashton J R, Castle K D, Qi Y, Kirsch D G, West J L and Badea C T 2018 Dual-Energy CT Imaging of Tumor Liposome Delivery After Gold Nanoparticle-Augmented Radiation Therapy *Theranostics* **8** 1782-97
- Ashton J R, Hoye J, Deland K, Whitley M, Qi Y, Moding E, Kirsch D G, West J and Badea C T Year *SPIE Medical Imaging*. A dual energy CT study on vascular effects of gold nanoparticles in radiation therapy, vol. Series 9788 p 8
- Ashton J R, West J L and Badea C T 2015 In vivo small animal micro-CT using nanoparticle contrast agents *Frontiers in pharmacology* **6** 256
- Badea C, Johnston S, Johnson B, Lin M, Hedlund L and Johnson G A Year *Medical Imaging 2008: Physics of Medical Imaging*. A dual micro-CT system for small animal imaging, vol. Series 6913 p 691342
- Badea C T, Athreya K K, Espinosa G, Clark D, Ghafoori A P, Li Y, Kirsch D G, Johnson G A, Annapragada A and Ghaghada K B 2012a Computed tomography imaging of primary lung cancer in mice using a liposomal-iodinated contrast agent *Plos One* **7** e34496

- 1
2
3 Badea C T, Guo X, Clark D, Johnston S M, Marshall C and Piantadosi C 2012b Lung imaging in rodents using dual
4 energy micro-CT *Proc Spie* **8317**
- 5 Badea C T, Holbrook M, Clark D P and Ghaghada K 2018 Spectral imaging of iodine and gadolinium nanoparticles
6 using dual-energy CT. In: *SPIE Medical Imaging: SPIE* p 7
- 7 Badea C T, Johnston S M, Qi Y, Ghaghada K and Johnson G A 2011 Dual energy micro-CT imaging for differentiation
8 of iodine and gold-based nanoparticles *Medical Imaging 2011: Physics of Medical Imaging* **7961**
- 9 Ballabriga R, Campbell M, Heijne E, Llopart X and Tlustos L Year 2006 *IEEE Nuclear Science Symposium Conference*
10 *Record*, The Medipix3 prototype, a pixel readout chip working in single photon counting mode with improved
11 spectrometric performance, vol. Series 6 pp 3557-61
- 12 Clark D, Touch M, Barber W and Badea C Year *Medical Imaging 2015: Physics of Medical Imaging*, Simultaneous
13 imaging of multiple contrast agents using full-spectrum micro-CT, vol. Series 9412 p 941222
- 14 Clark D P and Badea C T 2017 Hybrid spectral CT reconstruction *PLoS One* **12** e0180324
- 15 Clark D P, Ghaghada K, Moding E J, Kirsch D G and Badea C T 2013 In vivo characterization of tumor vasculature
16 using iodine and gold nanoparticles and dual energy micro-CT *Physics in medicine and biology* **58** 1683-704
- 17 Gao H, Yu H, Osher S and Wang G 2011 Multi-energy CT based on a prior rank, intensity and sparsity model (PRISM)
18 *Inverse Probl* **27**
- 19 Ghaghada K, Hawley C, Kawaji K, Annapragada A and Mukundan S, Jr. 2008 T1 relaxivity of core-encapsulated
20 gadolinium liposomal contrast agents--effect of liposome size and internal gadolinium concentration *Acad*
21 *Radiol* **15** 1259-63
- 22 Ghaghada K B, Badea C T, Karumbaiah L, Fetting N, Bellamkonda R V, Johnson G and Annapragada A 2011 Evaluation
23 of tumor microenvironment in an animal model using a nanoparticle contrast agent in computed tomography
24 imaging *Academic radiology* **18** 20-30
- 25 Ghaghada K B, Sato A F, Starosolski Z A, Berg J and Vail D M 2016 Computed Tomography Imaging of Solid Tumors
26 Using a Liposomal-Iodine Contrast Agent in Companion Dogs with Naturally Occurring Cancer *PLoS One*
27 **11** e0152718
- 28 Gierada D S and Bae K T 1999 Gadolinium as a CT contrast agent: Assessment in a porcine model *Radiology* **210** 829-
29 34
- 30 Gutjahr R, Halaweish A F, Yu Z, Leng S, Yu L, Li Z, Jorgensen S M, Ritman E L, Kappler S and McCollough C H
31 2016 Human Imaging With Photon Counting-Based Computed Tomography at Clinical Dose Levels:
32 Contrast-to-Noise Ratio and Cadaver Studies *Invest Radiol* **51** 421-9
- 33 Kirsch D G, Dinulescu D M, Miller J B, Grimm J, Santiago P M, Young N P, Nielsen G P, Quade B J, Chaber C J,
34 Schultz C P, Takeuchi O, Bronson R T, Crowley D, Korsmeyer S J, Yoon S S, Hornicek F J, Weissleder R
35 and Jacks T 2007 A spatially and temporally restricted mouse model of soft tissue sarcoma *Nat Med* **13** 992-
36 7
- 37 Lee C L, Min H, Befera N, Clark D, Qi Y, Das S, Johnson G A, Badea C T and Kirsch D G 2014 Assessing Cardiac
38 Injury in Mice With Dual Energy-MicroCT, 4D-MicroCT, and MicroSPECT Imaging After Partial Heart
39 Irradiation *Int J Radiat Oncol Biol Phys* **88** 686-93
- 40 Li Z, Leng S, Yu Z, Kappler S and McCollough C H 2016 Estimation of signal and noise for a whole-body photon
41 counting research CT system *Proc SPIE Int Soc Opt Eng* **9783**
- 42 Maeda H 2001 The enhanced permeability and retention (EPR) effect in tumor vasculature: the key role of tumor-
43 selective macromolecular drug targeting *Adv Enzyme Regul* **41** 189-207
- 44 Muenzel D, Bar-Ness D, Roessler E, Blevis I, Bartels M, Fingerle A A, Ruschke S, Coulon P, Daerr H, Kopp F K,
45 Brendel B, Thran A, Rokni M, Herzen J, Boussel L, Pfeiffer F, Proksa R, Rummeny E J, Douek P and Noel P
46 B 2017 Spectral Photon-counting CT: Initial Experience with Dual-Contrast Agent K-Edge Colonography
47 *Radiology* **283** 722-7
- 48 Mukundan S, Jr., Ghaghada K B, Badea C T, Kao C Y, Hedlund L W, Provenzale J M, Johnson G A, Chen E,
49 Bellamkonda R V and Annapragada A 2006 A liposomal nanoscale contrast agent for preclinical CT in mice
50 *AJR Am J Roentgenol* **186** 300-7
- 51 Radicci V, Commichau S, Donath T, Rissi M, Taniel Sakhelashvili, Schneebeli M, Traut S, Trueb P, Tudosie G and
52 Broennimann C First PILATUS3 200K-W CdTe detector: calibration and performance. Presented at the
53 International Workshop on Radiation Imaging Detectors iWoRID 2014, Trieste, Italy. Retrieved from
54 <https://agenda.cnaf.infn.it/getFile.py/access?contribId=132&resId=0&materialId=slides&confId=609>.
- 55 Rose A 1948 The sensitivity performance of the human eye on an absolute scale *J. Opt. Soc. Am.* **38** 196-208
- 56 Schlomka J P, Roessler E, Dorscheid R, Dill S, Martens G, Istel T, Baumer C, Herrmann C, Steadman R, Zeitler G, Livne
57 A and Proksa R 2008 Experimental feasibility of multi-energy photon-counting K-edge imaging in pre-clinical
58 computed tomography *Physics in medicine and biology* **53** 4031-47
- 59
60

- 1
2
3 Siewerdsen J H, Waese A M, Moseley D J, Richard S and Jaffray D A 2004 Spektr: a computational tool for x-ray
4 spectral analysis and imaging system optimization *Medical physics* **31** 3057-67
5 Starosolski Z, Villamizar C A, Rendon D, Paldino M J, Milewicz D M, Ghaghada K B and Annapragada A V 2015
6 Ultra High-Resolution In vivo Computed Tomography Imaging of Mouse Cerebrovasculature Using a Long
7 Circulating Blood Pool Contrast Agent *Sci Rep.* **5:10178**. 10.1038/srep10178.
8 Symons R, Pourmorteza A, Sandfort V, Ahlman M A, Cropper T, Mallek M, Kappler S, Ulzheimer S, Mahesh M,
9 Jones E C, Malayeri A A, Folio L R and Bluemke D A 2017 Feasibility of Dose-reduced Chest CT with
10 Photon-counting Detectors: Initial Results in Humans *Radiology* **285** 980-9
11 Taguchi K and Iwanczyk J S 2013 Vision 20/20: Single photon counting x-ray detectors in medical imaging *Medical*
12 *physics* **40** 100901
13 Zou W, Hunter N and Swain M V 2011 Application of polychromatic microCT for mineral density determination *J*
14 *Dent Res* **90** 18-30
15
16
17
18
19
20
21
22
23
24
25
26
27
28
29
30
31
32
33
34
35
36
37
38
39
40
41
42
43
44
45
46
47
48
49
50
51
52
53
54
55
56
57
58
59
60